



High-resolution periodic mode shapes identification for wind turbines

Riva, Riccardo; Cacciola, S; Croce, A

Published in:
Journal of Physics: Conference Series

Link to article, DOI:
[10.1088/1742-6596/1037/6/062002](https://doi.org/10.1088/1742-6596/1037/6/062002)

Publication date:
2018

Document Version
Publisher's PDF, also known as Version of record

[Link back to DTU Orbit](#)

Citation (APA):
Riva, R., Cacciola, S., & Croce, A. (2018). High-resolution periodic mode shapes identification for wind turbines. *Journal of Physics: Conference Series*, 1037(6), Article 062002. <https://doi.org/10.1088/1742-6596/1037/6/062002>

General rights

Copyright and moral rights for the publications made accessible in the public portal are retained by the authors and/or other copyright owners and it is a condition of accessing publications that users recognise and abide by the legal requirements associated with these rights.

- Users may download and print one copy of any publication from the public portal for the purpose of private study or research.
- You may not further distribute the material or use it for any profit-making activity or commercial gain
- You may freely distribute the URL identifying the publication in the public portal

If you believe that this document breaches copyright please contact us providing details, and we will remove access to the work immediately and investigate your claim.

PAPER • OPEN ACCESS

High-resolution periodic mode shapes identification for wind turbines

To cite this article: R Riva *et al* 2018 *J. Phys.: Conf. Ser.* **1037** 062002

View the [article online](#) for updates and enhancements.

Related content

- [Methodological approach to simulation and choice of ecologically efficient and energetically economic wind turbines \(WT\)](#)
Vadim Beshpalov, Natalya Udina and Natalya Samarskaya
- [Analysis of Counter-Rotating Wind Turbines](#)
W Z Shen, V A K Zakkam, J N Sørensen et al.
- [Effects of Icing on Wind Turbine Fatigue Loads](#)
Peter Frohboese and Andreas Anders

High-resolution periodic mode shapes identification for wind turbines

R Riva^{1,2}, S Cacciola², A Croce²

¹ Wind Energy Department, Technical University of Denmark, Frederiksborgvej 399, DK-4000 Roskilde, Denmark

² Dipartimento di Scienze e Tecnologie Aerospaziali, Politecnico di Milano, Via La Masa 34, 20156 Milano, Italy.

E-mail: ricriv@dtu.dk, stefano.cacciola@polimi.it, alessandro.croce@polimi.it

Abstract. The stability analysis of in-operation wind turbines is a very important topic, that has received considerable attention in the last years. Many identification algorithms have been developed to estimate frequencies and damping ratios, but very few papers have been dedicated to the mode shapes. The knowledge of high-resolution mode shapes could be exploited for several applications including model validation, accurate description of the vibratory content of a machine and spatially-accurate damage detection. In this work, we will present a procedure to compute the high-resolution periodic mode shapes of a wind turbine, and apply it to a high-fidelity wind turbine model. The results show that this methodology is able to identify the first low-damped modes of the system with good accuracy.

1. Introduction

An in-operation wind turbine is qualitatively different from a parked one since its motion makes it behave as a linear time-periodic (LTP) system. Many sources of periodicity can be listed as an example. The gravity causes a periodic stiffening of each blade. The vertical and horizontal wind shears periodically change the direction and magnitude of the aerodynamic loads. Advanced control laws, like the individual pitch control, cyclically change the pitch of the blades, further increasing the periodicity of the system. For these and other reasons, the stability analysis of an in-operation wind turbine, subject to a steady wind, should be conducted within a periodic framework, and hence by employing Floquet theory (see for example Ref. [1]).

The stability analysis of a wind turbine often aims at estimating only the frequencies and damping ratios, but it is nevertheless important to compute also the periodic mode shapes, which are typically used to justify the damping of certain modes or to compare models, as well as simulation codes. Recently, they have been used also to construct a damage indicator based on the loss of isotropy of the rotor [2].

To conduct the stability analysis, either model- or identification-based can be chosen. Among the first category, the most used technique is the Coleman approximation. This technique is fast, but introduces an error when the wind turbine is anisotropic. Moreover it cannot be applied to two-bladed rotors. An alternative technique is the implicit Floquet, which can capture the whole periodic content of the system but has a higher computational cost [3]. The majority of identification algorithms can identify only single-output systems and hence are inadequate to estimate the mode shapes with a high-resolution. The periodic mode shapes, of an in-operation



wind turbine, have been identified in Refs. [4, 5], but with a low resolution. In Refs. [6, 7], Yang identified the high-resolution mode shapes of wind turbine blades, but in those cases, the rotor was parked. A recent modal analysis of a parked wind turbine is provided also in Ref. [8]. To authors' knowledge, the periodic mode shapes of an in-operation wind turbine have never been identified with a high resolution, and in this paper, we will present a procedure to accomplish this task.

In Sec. 2 we will illustrate the identification procedure and the algorithms on which it is based. Sec. 3 will show a case study, and finally in Sec. 4 we will draw the conclusions.

2. Methodology

To identify the mode shapes of an in-operation wind turbine it is important to select an algorithm capable of identifying periodic systems having a large number of measurement channels. For this work, we have selected the Periodic PO-MOESP algorithm, originally presented by Felici in Ref. [9]. This algorithm belongs to the subspace methods, which are particularly suited to MIMO identification. The Periodic PO-MOESP can handle both process and measurement noises but has two limitations. First, it can identify only systems operating in open-loop, and second, it cannot capture the harmonics ($n \times \text{Rev}$), that characterize every wind turbine output. The first limitation makes it applicable only to stationary wind conditions, where the inputs of the system can be frozen before starting the identification process. The inability to capture the $n \times \text{Rev}$ requires instead a pre-processing step, aimed at removing these harmonics from the output. In Ref. [9] the authors proposed this algorithm to identify non-autonomous systems, assuming certain statistical properties of the inputs, which are hardly verified during a wind turbine field experiment. We thus propose to excite the wind turbine modes using an arbitrary impulse-like input sequence, remove the $n \times \text{Rev}$ from the output, and finally identify the system after the application of the input, i.e. from its free response. It can be verified that the Periodic PO-MOESP doesn't require any modification to handle this case. The stability of the identified system can be then assessed with the discrete-time Floquet theory.

In the subsequent part of this section, we will briefly explain the Periodic PO-MOESP, and the discrete-time Floquet theory.

2.1. The Periodic PO-MOESP identification algorithm

Let us consider the following autonomous linear time-periodic system

$$\mathbf{x}(k+1) = \mathbf{A}(k)\mathbf{x}(k) + \mathbf{F}(k)\mathbf{w}(k), \quad \mathbf{x}(0) = \mathbf{x}_0, \quad (1a)$$

$$\mathbf{y}(k) = \mathbf{C}(k)\mathbf{x}(k) + \mathbf{v}(k), \quad (1b)$$

with $\mathbf{x}(k) \in \mathbb{R}^{N_s}$ the state, and $\mathbf{y}(k) \in \mathbb{R}^\ell$ the output. $\mathbf{v}(k) \in \mathbb{R}^\ell$ is the measurement noise, and $\mathbf{w}(k) \in \mathbb{R}^z$ the process noise. Both $\mathbf{v}(k)$ and $\mathbf{w}(k)$ are by hypothesis zero-mean, white, and uncorrelated with the initial state \mathbf{x}_0 . The matrices $\mathbf{A}(k)$, $\mathbf{F}(k)$ and $\mathbf{C}(k)$ are all periodic with discrete-time period K . We will now write this system in a form that is commonly used for subspace identifications. To do so, we define the output array

$$\bar{\mathbf{y}}_k^d = (\mathbf{y}(k)^\top \quad \mathbf{y}(k+1)^\top \quad \cdots \quad \mathbf{y}(k+d-1)^\top)^\top \in \mathbb{R}^{\ell d \times 1}, \quad (2)$$

and similarly the arrays $\bar{\mathbf{w}}_k^d \in \mathbb{R}^{z d \times 1}$ and $\bar{\mathbf{v}}_k^d \in \mathbb{R}^{\ell d \times 1}$ for the process and measurement noise. The parameter d is named window size, and it must be $K \geq d > N_s$. The observability matrix for an

LTP system is defined as

$$\mathcal{O}_k^d = \begin{pmatrix} \mathbf{C}(k) \\ \mathbf{C}(k+1)\Phi(k+1, k) \\ \mathbf{C}(k+2)\Phi(k+2, k) \\ \vdots \\ \mathbf{C}(k+d-1)\Phi(k+d-1, k) \end{pmatrix} \in \mathbb{R}^{ld \times N_s}. \quad (3)$$

In the following we will assume that the system is observable for all k , over a length d , so that \mathcal{O}_k^d has full column rank, i.e. $\text{rank}(\mathcal{O}_k^d) = N_s$. We then define

$$\mathcal{E}_k^d = \begin{pmatrix} \mathbf{0} & \mathbf{0} & \cdots & \mathbf{0} & \mathbf{0} \\ \mathcal{E}_{k,2,1}^d & \mathbf{0} & \cdots & \mathbf{0} & \mathbf{0} \\ \mathcal{E}_{k,3,1}^d & \mathcal{E}_{k,3,2}^d & \cdots & \mathbf{0} & \mathbf{0} \\ \vdots & \vdots & \ddots & \mathbf{0} & \mathbf{0} \\ \mathcal{E}_{k,d,1}^d & \mathcal{E}_{k,d,2}^d & \cdots & \mathcal{E}_{k,d,d-1}^d & \mathbf{0} \end{pmatrix} \in \mathbb{R}^{ld \times zd}, \quad (4)$$

with $\mathcal{E}_{k,i,j}^d = \mathbf{C}(k+i-1)\Phi(k+i-1, k+j)\mathbf{F}(k+j-1)$, for $i = 2, \dots, d$, $j = 1, \dots, d-1$ and $i > j$. Because of the periodicity of the system, it can be verified that $\mathcal{O}_k^d = \mathcal{O}_{k+K}^d$ and $\mathcal{E}_k^d = \mathcal{E}_{k+K}^d$, $\forall k \in \{0, \dots, \bar{N}-1\}$, with \bar{N} the number of periods. By making use of these definitions we can see that

$$\bar{\mathbf{y}}_k^d = \mathcal{O}_k^d \mathbf{x}(k) + \mathcal{E}_k^d \bar{\mathbf{w}}_k^d + \bar{\mathbf{v}}_k^d, \quad \forall k \in [0, \dots, N-1], \quad (5)$$

with $N = \bar{N}K$ the number of samples. To get the output over all the periods we define the data matrix

$$\bar{\mathbf{Y}}_k^{i,d,\bar{N}} = \begin{pmatrix} \bar{\mathbf{y}}_{k+iK}^d & \bar{\mathbf{y}}_{k+(i+1)K}^d & \cdots & \bar{\mathbf{y}}_{k+(i+\bar{N}-1)K}^d \end{pmatrix} \in \mathbb{R}^{ld \times \bar{N}}. \quad (6)$$

Analogously we define $\bar{\mathbf{V}}_k^{i,d,\bar{N}} \in \mathbb{R}^{ld \times \bar{N}}$ and $\bar{\mathbf{W}}_k^{i,d,\bar{N}} \in \mathbb{R}^{zd \times \bar{N}}$ for the process and measurement noise. For the state we introduce

$$\bar{\mathbf{X}}_k^{i,\bar{N}} = \begin{pmatrix} \mathbf{x}(k+iK) & \mathbf{x}(k+(i+1)K) & \cdots & \mathbf{x}(k+(i+\bar{N}-1)K) \end{pmatrix} \in \mathbb{R}^{N_s \times \bar{N}}, \quad (7)$$

so that the output can finally be computed as

$$\bar{\mathbf{Y}}_k^{i,d,\bar{N}} = \mathcal{O}_k^d \bar{\mathbf{X}}_k^{i,\bar{N}} + \mathcal{E}_k^d \bar{\mathbf{W}}_k^{i,d,\bar{N}} + \bar{\mathbf{V}}_k^{i,d,\bar{N}}, \quad \forall k \in [0, \dots, K-1]. \quad (8)$$

The Periodic PO-MOESP aims at identifying the observability matrix by exploiting the data matrix. In Ref. [9] it is proved that if

$$\text{rank} \left(\lim_{\bar{N} \rightarrow \infty} \frac{1}{\bar{N}} \bar{\mathbf{X}}_{k+K-d}^{0,\bar{N}} \right) = N_s, \quad \text{and} \quad \text{rank} \left(\lim_{\bar{N} \rightarrow \infty} \frac{1}{\bar{N}} \bar{\mathbf{X}}_k^{1,\bar{N}} (\bar{\mathbf{Y}}_{k+K-d}^{0,d,\bar{N}})^\top \right) = N_s \quad (9)$$

then it holds that

$$\text{range} \left(\lim_{\bar{N} \rightarrow \infty} \frac{1}{\bar{N}} \bar{\mathbf{Y}}_k^{1,d,\bar{N}} (\bar{\mathbf{Y}}_{k+K-d}^{0,d,\bar{N}})^\top \right) = \text{range}(\mathcal{O}_k^d). \quad (10)$$

These equations show that if the state has been properly excited, then the range of the observability matrix equals the one of the matrix in the left hand side of Eq. (10). As done in Ref. [9], rather than computing the matrix product in Eq. (10), we perform the following LQ decomposition

$$\begin{pmatrix} \bar{\mathbf{Y}}_{k+K-d}^{0,d,\bar{N}} \\ \bar{\mathbf{Y}}_k^{1,d,\bar{N}} \end{pmatrix} = \begin{pmatrix} \mathbf{L}_{k11} & \mathbf{0} \\ \mathbf{L}_{k21} & \mathbf{L}_{k22} \end{pmatrix} \begin{pmatrix} \mathbf{Q}_{k1} \\ \mathbf{Q}_{k2} \end{pmatrix}, \quad (11)$$

in which the factors $\mathbf{L}_{k_{11}}$, $\mathbf{L}_{k_{21}}$ and $\mathbf{L}_{k_{22}}$ have size $d\ell \times d\ell$, while \mathbf{Q}_{k_1} and \mathbf{Q}_{k_2} have size $d\ell \times \bar{N}$. In Ref. [9] it is proved that

$$\text{range} \left(\lim_{\bar{N} \rightarrow \infty} \frac{1}{\sqrt{\bar{N}}} \mathbf{L}_{k_{21}} \right) = \text{range} (\mathcal{O}_k^d). \quad (12)$$

The range of the observability matrix is then obtained by computing the Singular Value Decomposition of $\mathbf{L}_{k_{21}}$

$$\mathbf{L}_{k_{21}} = \mathbf{U}_k \text{diag}(\boldsymbol{\sigma}_k) \mathbf{V}_k^T. \quad (13)$$

The order of the system can be estimated for each k by looking at a possible gap in the singular values $\boldsymbol{\sigma}_k$, while the first N_s columns of \mathbf{U}_k provide the desired range. To compute the LQ decomposition of Eq. (11), it is required that $\bar{N} \geq 2d\ell$. Often this condition requires to measure the system for a very long time. It is however possible to measure the system till its free response has vanished, and then simply zero-pad the measures. In this way the measurement time is dictated by the physics of the system, rather than by the identification algorithm. The side effect of this technique, is that the elements of $\boldsymbol{\sigma}_k$ after the last measured period assume the value of the machine ϵ .

The matrices of the system are obtained by exploiting the structure of the observability matrix. The first ℓ rows of the observability matrix are simply the output matrix. Therefore, by indicating with $\mathbf{M}(i:j,:)$ the selection from row i to row j of matrix \mathbf{M} , we can write

$$\tilde{\mathbf{C}}(k) = \mathbf{U}_k(1:\ell,:), \quad \forall k \in [0, \dots, K-1]. \quad (14)$$

The $\mathbf{A}(k)$ matrix is instead found by solving

$$\mathbf{U}_{k+1}(1:\ell(d-1),:)\mathbf{A}_k = \mathbf{U}_k(\ell+1:\ell d,:), \quad \forall k \in [0, \dots, K-1], \quad (15)$$

in the least-squares sense. Lastly, we write Eq. (5) at the initial time, to get the initial state. Since both noises are by hypothesis white, we can omit them, and write

$$\bar{\mathbf{y}}_0^d = \mathcal{O}_0^d \mathbf{x}_0. \quad (16)$$

We thus have

$$\mathbf{x}_0 = \mathbf{U}_0(:, 1:N_s)^\dagger \bar{\mathbf{y}}_0^d, \quad (17)$$

where $\mathbf{M}(:, k:l)$ indicates the selection from column k to column l , and $(\cdot)^\dagger$ is the matrix pseudoinverse.

2.2. Stability analysis of linear discrete-time periodic systems

The stability analysis of system (1) is performed by applying Floquet theory, see Ref. [1, 10], and in this paragraph we will provide a concise review of it.

The motion of $\mathbf{x}(k)$, and hence the stability of a periodic system, is governed by the state transition matrix $\Phi(k, \kappa)$ which evolves according to

$$\Phi(k+1, \kappa) = \mathbf{A}(k)\Phi(k, \kappa), \quad \Phi(\kappa, \kappa) = \mathbf{I}, \quad (18)$$

with \mathbf{I} the identity matrix. By sampling the state at every period, we can see that its motion is governed by the monodromy matrix $\Psi_\kappa = \Phi(\kappa + K, \kappa)$. The eigenvalues θ_j of Ψ_κ are termed characteristic multipliers, and the system is asymptotically stable if they lie within the open unit disk, i.e. if

$$|\theta_j| < 1, \quad \forall j \in [1, \dots, N_s]. \quad (19)$$

By neglecting the noise, the output of system (1) can be computed as

$$\mathbf{y}(k) = \mathbf{C}(k)\mathbf{\Phi}(k, \kappa)\mathbf{x}(\kappa), \quad (20)$$

where $\mathbf{C}(k)\mathbf{\Phi}(k, \kappa)$ is named observed state transition matrix. It can be proved that the modal decomposition of this matrix is given by

$$\mathbf{C}(k)\mathbf{\Phi}(k, \kappa) = \sum_{j=1}^{N_s} \sum_{n=0}^{K-1} \boldsymbol{\psi}_{j_n} \boldsymbol{\varrho}_j^{\top}(\kappa) (\eta_{j_n})^{k-\kappa} e^{i n \frac{2\pi}{K} \kappa}, \quad (21)$$

with

$$\eta_{j_n} = \sqrt[K]{|\theta_j|} \exp\left(i \frac{\angle(\theta_j) + 2n\pi}{K}\right) \quad (22)$$

and $i = \sqrt{-1}$. Equation (21) shows that each mode j is characterized by K harmonics, composed by the characteristic exponents η_{j_n} , and by the associated observed periodic mode shapes $\boldsymbol{\psi}_{j_n}$. To assess the relative importance of each harmonic within a specified mode, we introduce the output-specific participation factor

$$\phi_{j_n} = \frac{\|\boldsymbol{\psi}_{j_n}\|_2}{\sum_n \|\boldsymbol{\psi}_{j_n}\|_2}. \quad (23)$$

When selecting as reference frame the multi-blade coordinates, the harmonic with the highest ϕ_{j_n} is labeled principal. The characteristic exponents play the same role of the eigenvalues of a linear time-invariant system, and can be converted in continuous time with

$$\eta_{j_n}^{\text{cont.}} = \frac{1}{\Delta t} \ln(\eta_{j_n}) \quad (24)$$

where Δt is the time step. The natural frequencies f_{j_n} and damping ratios ξ_{j_n} are obtained as

$$f_{j_n} = \frac{|\eta_{j_n}^{\text{cont.}}|}{2\pi}, \quad \xi_{j_n} = -\frac{\text{Re}(\eta_{j_n}^{\text{cont.}})}{|\eta_{j_n}^{\text{cont.}}|}. \quad (25)$$

3. Application to the AVATAR wind turbine

The proposed procedure has been applied to a 10 MW, low induction rotor, wind turbine, developed within an European project AVATAR [11, 12]. The wind turbine has been modeled with the Cp-Lambda code [13], an aero-servo-elastic code based on a multi-body formulation. The beam model is geometrically exact, with a fully-populated stiffness matrix, able to correctly capture the behavior of modern, composite-made, wind turbine blades. The aerodynamics is rendered through the classical blade-element momentum theory, with the quasi-steady approximation. The aerodynamic model includes tip and hub losses and the tower shadow. To identify the system 20 displacement sensors have been applied on each blade, in order to measure the edgewise displacement relative to the root. Moreover, other 20 sensors have been considered on the tower, to get the side-side displacement. During a real experiment, the displacements might be measured with the stereo photometry, as described, for instance, in Ref. [14].

To simulate the system we have applied a Normal Wind Profile, with a vertical wind shear exponent of 0.20 and a speed at the hub height of 13 m/s. After the system reached a trim condition, the pitch and torque have been frozen, so as to simulate an open-loop system.

3.1. Identification of the tower side-side mode

To identify the tower side-side mode, we have applied a force at the tower top, in the side-side direction. The force had the trend of a doublet, with a duration tuned to excite the principal harmonic of this mode. To ease the identification process we have applied the Coleman transformation (see Ref. [10]), which had a two-fold effect. First it filtered all the $n \times \text{Rev}$ where n is not a multiple of 3, while the second is that in multi-blade coordinates this mode is characterized almost exclusively by its principal harmonic. In this way we have been able to do a more aggressive pre-processing, to better remove the remaining $n \times \text{Rev}$ as well as some high-frequency oscillations.

The singular values revealed that the rank of the observability matrix is constant over the period, and equal to 2, therefore we set $N_s = 2$. By a trial and error approach we have set the window size d equal to the discrete-time period, so that no information is discarded. The measures in the physical frame are retrieved by applying the inverse Coleman transformation to the $\mathbf{C}(k)$ matrix.

Table 1 lists the identified frequencies and damping ratios, with the associated output-specific participation factors. The participation factors indicate that this mode manifests only with its principal harmonic in the fixed frame, of which we show the mode shape, observed on the tower, in the central column of Fig. 1. Instead, in the rotating frame this mode manifests with the $\pm\Omega$ harmonics. The mode shapes of these harmonics, observed on the blades, are shown in the left and right columns of Fig. 1. Eq. (21) shows that for periodic systems the scaling factor of the mode shapes depends only on the mode, and not on the harmonic. Hence, in all the figures we have normalized to 1 the maximum displacement among all the harmonics, and scaled the other harmonics accordingly. As we can see, the $+\Omega$ harmonic is the least damped, and is experienced by the blades. Moreover, the mode shapes of the blades have the same magnitude, with phases constant along the span, and separated by about 120° .

Table 1: Frequencies, damping ratios, and output-specific participation factors of the tower side-side mode.

Harmonic	Frequency (Hz)	Damping (-)	Participation	
			Tower top	Blade 1 tip
-1Ω	0.063	0.0253	0.0001	0.4638
Principal	0.223	0.0072	0.9953	0.0082
$+1\Omega$	0.383	0.0042	0.0012	0.5020

3.2. Identification of the edgewise collective mode

For this identification we have applied a torque to the shaft. The torque had the trend of a doublet, with a duration tuned to excite mainly the principal harmonic of this mode. For this mode the motion of the tower is very limited, therefore we have excluded its signals from the identification. In this case, we have chosen to keep the measures in the rotating frame, since the Coleman transformation is not appropriate for this mode. We have then removed the $n \times \text{Rev}$, and applied a high-pass filter, to clean the spectrum below 1.4 Hz.

The identified frequencies and damping ratios are listed in Tab. 2. The participation factors reveal that only the principal harmonic is important to describe this mode, and we show its mode shape in Fig. 2. Once again, the mode shapes of the blade have the same magnitude, but in this case also the phases are equal, coherently with the definition of collective mode.

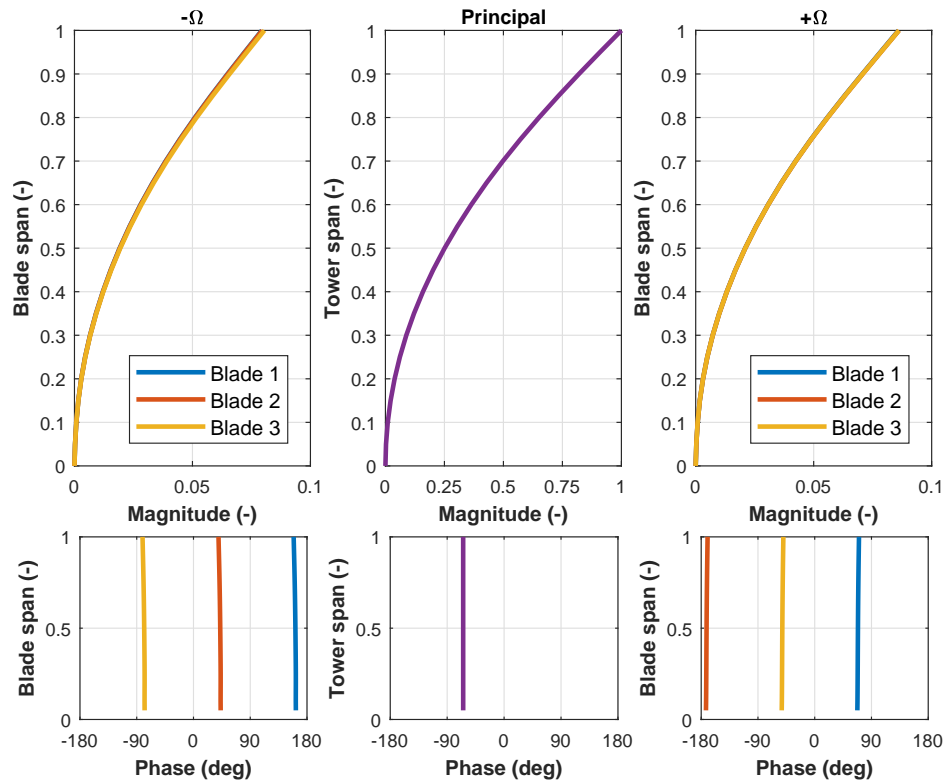


Figure 1: Observed periodic mode shapes of the tower side-side mode.

Table 2: Frequencies, damping ratios, and output-specific participation factors of the edgewise collective mode.

Harmonic	Frequency (Hz)	Damping (-)	Participation Blade 1 tip
-1Ω	1.487	0.0407	0.0095
Principal	1.647	0.0368	0.8181
$+1\Omega$	1.806	0.0335	0.0042

3.3. Identification of the edgewise whirling modes

The last identification concerned the edgewise whirling modes. In this case we have applied three concentrated forces at the tip of the blades. Each force was orthogonal to the associated blade axis, and lied in the rotor plane. The forces had different magnitude and start time, but they all had the trend of a doublet, tuned to excite the whirling modes as observed in the rotating frame. This type of forcing not only excites the edgewise whirling modes, but also the collective edgewise and the tower side-side modes, although the latter is not visible on the blades.

In Ref. [15] it is explained that the whirling modes respond with the same frequency when they are observed in the rotating frame, and with two different ones when observed in multi-blade coordinates. Therefore, to facilitate the identification, we have applied the Coleman transformation. The Periodic PO-MOESP allowed to identify a system that incorporates all of these modes, except for the collective edgewise.

Tab. 3 lists the identified frequencies and damping ratios, along with the associated output-specific participation factors, of the edgewise backward whirling mode. The participation factors indicate that the principal harmonic is observed on the tower, of which we draw the mode shape

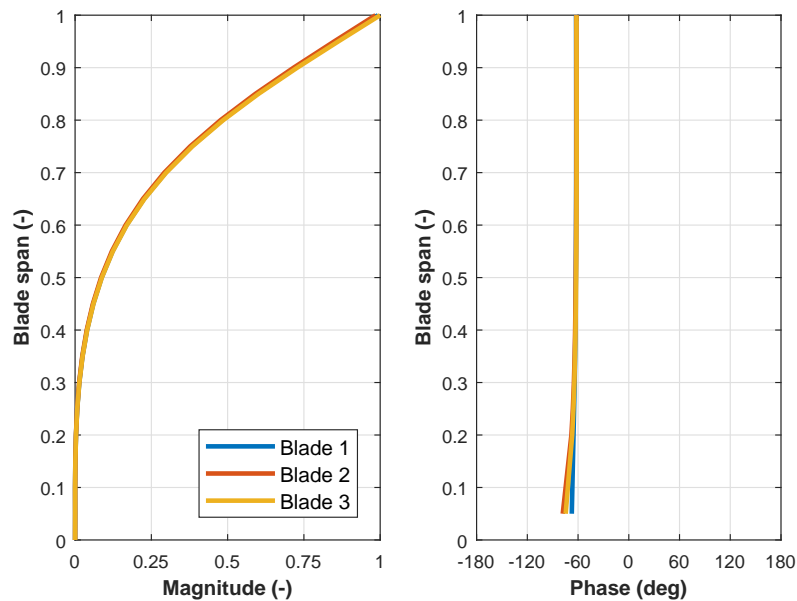


Figure 2: Observed periodic mode shape of the principal harmonic of the edgewise collective mode.

in the left column of Fig. 3. On the blades it is instead observed the $+\Omega$ harmonic, whose mode shape is shown in the right column of Fig. 3. As discussed in Ref. [3], for the whirling modes the phases of the blades are constant along the span, and separated by about 120° . In the Campbell diagram often it is shown only the principal harmonic, however, the ample difference in displacement among the blades and tower indicates that the most important harmonic for this mode is the $+\Omega$.

Table 3: Frequencies, damping ratios, and output-specific participation factors of the edgewise backward whirling mode.

Harmonic	Frequency (Hz)	Damping (-)	Participation	
			Tower top	Blade 1 tip
-1Ω	0.5738	0.0301	0.0009	0.0196
Principal	0.7337	0.0235	0.7674	0.0034
$+1\Omega$	0.8937	0.0193	0.0012	0.8025

Analogous considerations apply for the edgewise forward whirling mode. The results for its identification are shown in Tab. 4 and Fig. 4.

Table 4: Frequencies, damping ratios, and output-specific participation factors of the edgewise forward whirling mode.

Harmonic	Frequency (Hz)	Damping (-)	Participation	
			Tower top	Blade 1 tip
-1Ω	0.8924	0.0308	0.0044	0.3409
Principal	1.0523	0.0261	0.3905	0.0042
$+1\Omega$	1.2122	0.0226	0.0070	0.0044

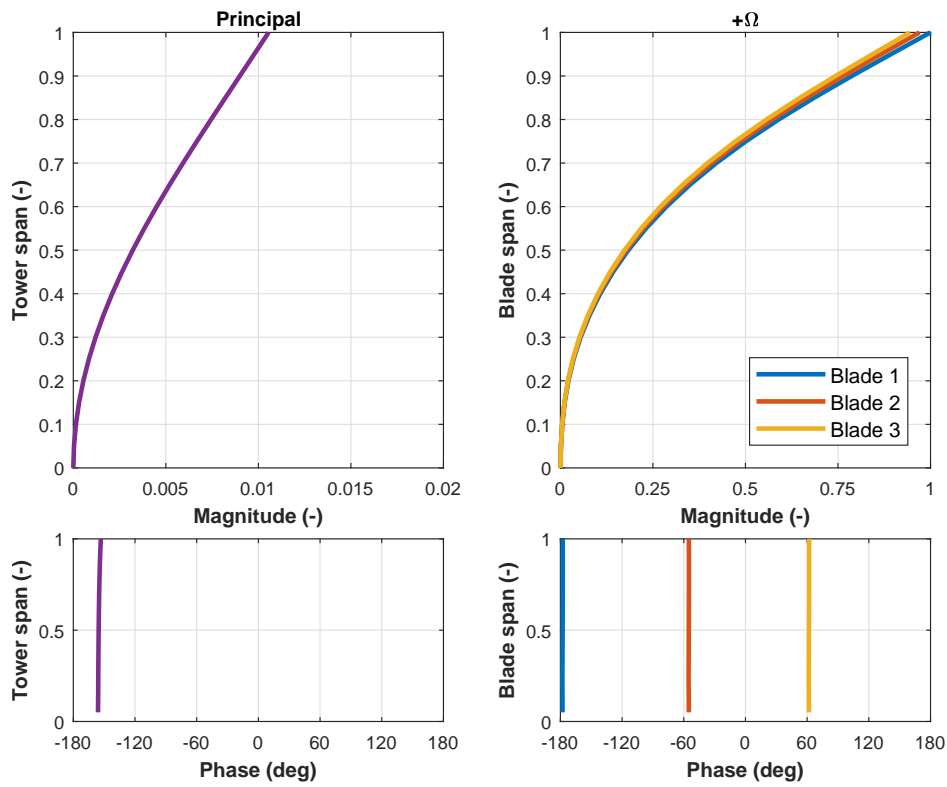


Figure 3: Observed periodic mode shapes of the edgewise backward whirling mode.

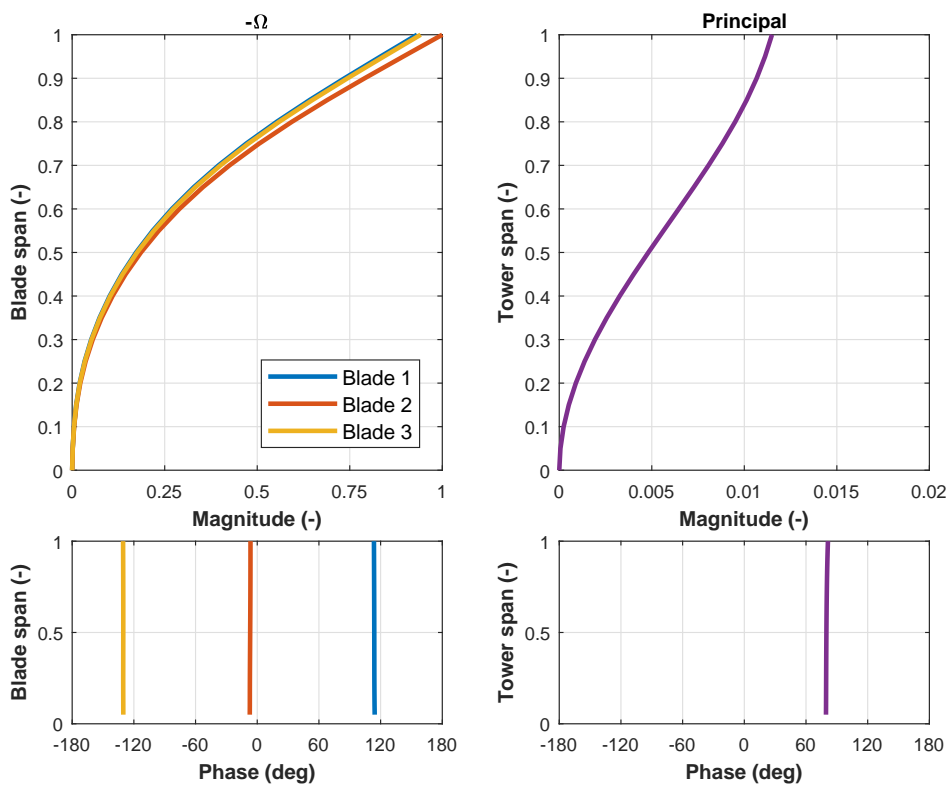


Figure 4: Observed periodic mode shapes of the edgewise forward whirling mode.

4. Conclusion

In this paper, we have presented a procedure to identify high-resolution periodic mode shapes of an in-operation wind turbine. The procedure relies on the Periodic PO-MOESP identification algorithm, which we have specifically tailored for this purpose. This algorithm produces a reduced order model, whose stability is assessed by the discrete-time Floquet theory, this way considering the whole periodic content of the system. The procedure, being based on system identification, is model-independent and applicable to any simulation model of arbitrary complexity.

As a case study, we have conducted virtual experiments, to estimate the mode shapes of the AVATAR wind turbine. In particular, we have identified the first low-damped modes of the system with good accuracy. The results include the most important harmonics for each mode and show that the least-damped harmonic might not be the one usually shown in a Campbell diagram.

The methodology proposed in this work allows one to better compare different models and simulation codes. Future works will concern the inclusion of control system and turbulence in the identification process, so as to make it applicable to more realistic scenarios.

Acknowledgments

This work has been partially supported by the AVATAR project, which received funding from the European Union's Seventh Programme for research, technological development and demonstration under grant agreement No FP7-ENERGY-2013-1/no. 608396.

References

- [1] Riva R, Cacciola S and Bottasso C L 2016 Periodic stability analysis of wind turbines operating in turbulent wind conditions *Wind Energy Science* **1** 177–203
- [2] Tcherniak D 2016 Rotor anisotropy as a blade damage indicator for wind turbine structural health monitoring systems *Mech. Syst. Signal Pr.* **74** 183–198
- [3] Skjoldan P F and Hansen M H 2011 Implicit Floquet analysis of wind turbines using tangent matrices of a non-linear aeroelastic code *Wind Energy* **15** 275–287
- [4] Allen M S, Sracic M W, Chauhan S and Hansen M H 2011 Output-only modal analysis of linear time-periodic systems with application to wind turbine simulation data *Mech. Syst. Signal Pr.* **25** 1174–91
- [5] Yang S, Tcherniak D and Allen M S 2014 Modal analysis of rotating wind turbine using multiblade coordinate transformation and harmonic power spectrum *Topics in Modal Analysis I, Volume 7* De Clerck J (Springer, Cham) pp 77–92
- [6] Yang S and Allen M S 2012 Output-only Modal Analysis using continuous-scan laser doppler vibrometry and application to a 20kW wind turbine *Mech. Syst. Signal Pr.* **31** 228–45
- [7] Yang S and Allen M S 2012 Lifting approach to simplify output-only continuous-scan laser vibrometry *Mech. Syst. Signal Pr.* **45** 267–82
- [8] Zierath J *et al.* 2018 Experimental identification of modal parameters of an industrial 2-MW wind turbine *Wind Energy* 1–19
- [9] Felici F, Van Wingerden J-W and Verhaegen M 2007 Subspace identification of MIMO LPV systems using a periodic scheduling sequence *Automatica* **43** 1684–97
- [10] Skjoldan P F and Hansen M H 2009 On the similarity of the Coleman and Lyapunov–Floquet transformations for modal analysis of bladed rotor structures *J. Sound. Vib.* **327** 424–39
- [11] Schepers J G *et al.* 2015 AVATAR: AdVanced Aerodynamic Tools of lArge Rotors 33rd Wind Energy Symposium AIAA SciTech Forum
- [12] Schepers J G *et al.* 2016 Latest results from the EU project AVATAR: Aerodynamic modelling of 10 MW wind turbines *J. Phys.: Conf. Ser.* **753** 022017
- [13] Bottasso C L and Croce A 2006 Cp-Lambda: user's manual *Dipartimento di Scienze e Tecnologie Aerospaziali, Politecnico di Milano*
- [14] Najafi N and Vesth A 2017 Establishing a robust testing approach for displacement measurement on a rotating horizontal axis wind turbine *Wind Energ. Sci. Discuss. Preprint*
- [15] Hansen M H 2007 Aeroelastic instability problems for wind turbines *Wind Energy* **10**(6) 551–77